ORIGINAL ARTICLE

Luminescence in Er^{3+} co-doped bismuth germinate glass–ceramics for blue and green emitting applications

I. Kashif[2] · A. Ratep[1]

Abstract

Glass samples with the composition 40 Bi$_2$O$_3$-60 GeO$_2$-x Er$_2$O$_3$ are prepared using the melt quenching procedure. Fourier-transform infrared spectroscopy (FTIR), differential thermal analysis (DTA), Ultraviolet/Visible/Near-infrared (UV/Vis–NIR) absorption, photoluminescence spectroscopy (PL), and X-ray diffraction (XRD) are used to characterize the glass and glass–ceramic materials. The glass transition and crystallization temperatures are determined. Crystallization kinetics was studied in non-isothermal conditions. The oscillator strengths and Judd–Ofelt parameters (Ω_2, Ω_4, Ω_6) for reported Er^{3+} absorption transitions are estimated, and they follow the trend $\Omega_2 > \Omega_6 > \Omega_4$ for observed Er^{3+} absorption transitions. The iconicity of glass samples was unaffected by an increase in Er^{3+} ions. XRD and FTIR confirmed the formation of the Bi$_4$Ge$_3$O$_{12}$ phase after heat treatment of glass samples at the crystallization temperature. The CIE chromaticity diagram computes the CIE chromatic coordinates. The values for all glass and crystal samples are close to bright blue and green. Glass and glass ceramic samples are suitable for green and blue optoelectronics device applications.

Keywords Glass · Ceramic · Infrared (IR) spectroscopy · Differential thermal analysis (DTA) · Luminescence · Optical properties · X-ray diffraction (XRD)

1 Introduction

The glass crystal system offers two distinct advantages. It functions as a glass composition with various rare-earth or transition metal compositions. Glass samples containing rare-earth ions are of great interest due to their many practical and potential applications.

Due to the high conversion process of converting infrared rays into visible light and flat screens, which uses as glass lasers, optical fiber amplifiers, phosphors, electroluminescent devices, and memory devices [1, 2].

The application of bismuth and germanium in glass is significant because it uses as a layer for optical and optoelectronic devices, thermal and mechanical sensors, infrared transmitting windows, and active media for Raman optical fiber amplifiers. Due to its outstanding structural characteristics, this glass system uses in a wide range of fields [1], temperature sensors, 1.55 m amplifications, and planar waveguides [3]. The other method converts glass into a crystal phase through heat treatment. The crystal phase that results from this procedure has the same properties as a single crystal. It also has the advantages of being inexpensive and simple to make. Bismuth germinate oxide is a component of the glass–ceramic system.

The crystalline phase generates by heat treatment and is controlled by many parameters, such as the ratio of bismuth to germanium oxide, the melting temperature, and cooling rates [4].

Many researchers directed their attention to the preparation of bismuth germinate glasses and the Bi$_4$Ge$_3$O$_{12}$ phase. According to their physical properties, they can use optical waveguides in the IR (infrared) region, as well as active media for Raman optical fiber, scintillation counters, thermal and mechanical sensors, as well as other optical devices, such as optical fibers, optical switching, and optical memory [1, 5].

✉ I. Kashif
ismailkashif52@yahoo.com; ismailkashif@azhar.edu.eg

A. Ratep
assmakalifa@yahoo.com; asmaa.ratep@women.asu.edu.eg

1 Faculty of Women for Art, Science and Education, Department of Physics, Ain Shams University, Heliopolis, Cairo, Egypt

2 Faculty of Science, Department of Physics, Al-Azhar University, Nasr City, Cairo, Egypt

Chen et al. and Sanghi et al. [6, 7] have studied and compared the optical properties of different glass formations, such as bismuth glass, borate glass, and commercial laser glass doped with Er^{3+} ions. From this study, the researchers concluded that the spectral parameters of bismuth borate glass are better than those of other glasses.

Polosan et al. [8] investigated the melt-quenched glass-controlled crystallization of bismuth–germinate glass ($40Bi_2O_3$–60 GeO_2 mol %). And found that the formed phase affected by the annealing of the glass sample above the crystallization temperature (558 °C) formed the $Bi_4Ge_3O_{12}$ nano and traces of Bi_2GeO_5 crystallites. The number of nanocrystals grows as the annealing temperature rises, while their size remains constant in the 50 nm range.

Polosan et al. [9] investigated the production of $Bi_4Ge_3O_{12}$ (BGO) from a combination of oxides at 1323 K. The optical characteristics and dielectric functions of a sample made using BGO single crystals were compared.

In this article, we direct our efforts toward studying glass samples prepared in two steps: firstly, study the glass structure and determine the physical, thermal, optical, and emission properties, and determine the effect of adding Er_2O_3. Secondly, investigate the production and characteristics of the $Bi_4Ge_3O_{12}$ phase.

2 Experimental work

Glass samples having a composition of 40 Bi_2O_3-60 GeO_2-x Er_2O_3 mol%, created with x=0, 0.5, 1.0, 1.5, and 2 mol%. The samples were placed in an oven at 1100 °C for one h., a molten poured between two copper plates in the air. XRD system from Philips Analytical (type PW3710) used a Cu tube anode with wavelengths of $K_{\alpha1}$ =1.54060 and $K_{\alpha2}$ =1.54439 to examine the nature of all samples. The starting angle (2θ) was 10°, and the ending was 70°. The FTIR JASCO, 6300 infrared spectrometer using to measure the absorption spectra in the range of 400–4000 cm^{-1} of all samples using the KBr pellets technique. The prepared samples were analyzed using differential thermal analysis (DTA) at temperatures ranging from 30 to 1200 °C, with heating rates of 5, 10, 20, and 30 °C/min, and Al_2O_3 powder as a reference material (Shimadzu DTA-50 analyzer) measured. A computerized recording spectrophotometer uses to measure the optical transmission spectra in the region of 190 to 2500 nm (JASCO, V-570). The emission measurements were calculated by using the (JASCO–FP-6300) Spectrofluorometer in the (200–800 nm) wavelength range.

3 Results and discussion

3.1 XRD

The state of the samples is amorphous or crystalline examined using XRD equipment. Fig. 1 reveals that the XRD pattern of the materials under analysis is devoid of identifiable peaks.

Figure 1 indicates that the samples are amorphous.

3.2 FTIR

FTIR is a guide instrument that detects any structural changes formed in the vibration groups of the glass network. Fig. 2 shows the glass free of Er, an obvious band for Bi and Ge beginning at 475 cm^{-1}, representing Bi-O vibration in BiO_6 [10]. The band at 540 cm^{-1} represents the distorted BiO_6 [1, 11]. The bands around 560–580 cm^{-1} and 1045 cm^{-1} represent the stretching vibration of GeO_4 overlapped with the BiO_6 vibration band [1, 10]. The two bands at 730 cm^{-1} and 770 cm^{-1} represent the stretching of GeO_4 [1]. The band at 860 cm^{-1} represents BiO_6 [1] and the asymmetric stretching of GeO_4 [10]. The band at 1035 cm^{-1} indicates the stretching band of Ge–O in GeO_4 [1]. The band at 1100 cm^{-1} represents the Bi-O-Bi bond or Bi-O-Ge [1]. The first addition of Er_2O_3 begins to appear in several bands as the band at 495 cm^{-1} represents the BiO_6 octahedral units [7, 12] or the bending vibration of BiO_3 units [1]. A little band at 600 Cm^{-1} represents the Bi-O- stretching vibration in BiO6 [1]. The band at 443 cm^{-1} was attributed to symmetry stretching of bridging oxygen (BO) in 6-membered GeO_4 rings Ge–O–Ge [13], and the continuous addition of Er broadened the band and could include bands. The
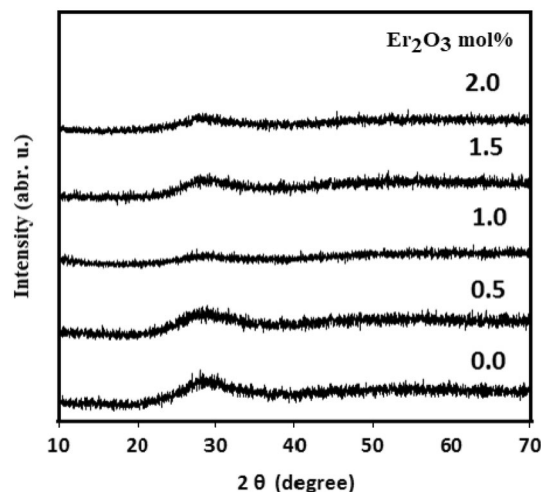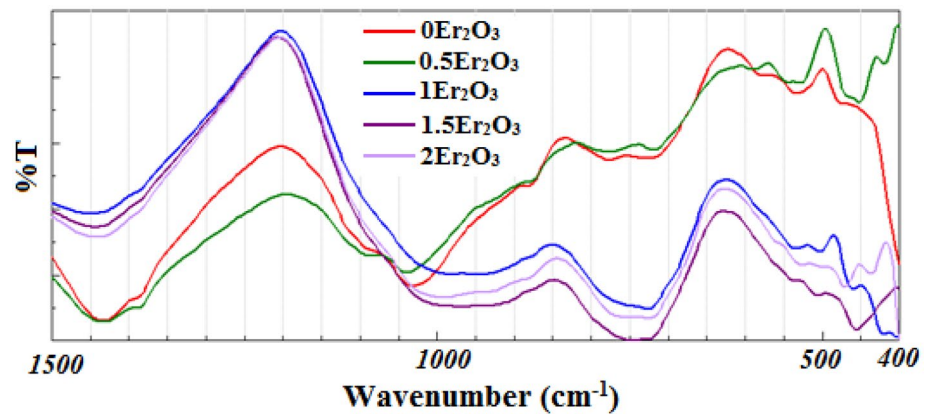

Fig. 1 XRD for glass samples prepared

Fig. 2 FTIR spectra of prepared glass sample

appearance of a new band at 520 cm^{-1} represents the defect mode of GeO$_4$ [13], while the band at 630 Cm^{-1} represents the stretching of BiO$_6$. The bands at 710–750 cm^{-1} represent GeO$_4$ [1]. The band at 845 cm^{-1} corresponds to the symmetric stretching of BiO$_3$ [1, 7], while the band ranging from 750 to 900 cm^{-1} corresponds to the Bi-O stretching vibration in BiO$_3$ units [11] and the asymmetric stretching of bridging oxygen in Ge–O–Ge [13].

As for undoped and Er-doped Bi$_2$O$_3$-GeO$_2$ glass samples, there are broadband located between 850 cm^{-1} and 1200 cm^{-1}, which should be corresponding to the vibrations of 850 to 930 cm^{-1}, 1016 to 1031 cm^{-1} and 1090 to 1110 cm^{-1}, respectively. However, the line shape of the vibrations becomes broad compared to that of the 2Bi$_2$O$_3$-3GeO$_2$ glass sample, which suggests that the structures of 2Bi$_2$O$_3$-$_3$GeO$_2$ and Er-doped Bi$_2$O$_3$-GeO$_2$ are slightly different. With the deconvolution the broad bands consist of three bands at of 850 to 930 cm^{-1}, 1016 to 1031 cm^{-1} and 1090 to 1110 cm^{-1}. Fig. 3 shows the effect of Er$_2$O$_3$ addition on these bands. From Fig. 3, observed the Bi–O–Ge linkage (1090 to 1110 cm^{-1}) decreases and the vibration of Bi–O bonds in BiO6 units and Ge–O–Ge

asymmetric stretching of GeO4 increases as Er$_2$O$_3$ equal and greater than 1 mol %, while GeO4 vibration groups (1016 to 1031) constant for all samples. It is clear the structure variation between samples.

3.3 Optical absorption

Figure 4 depicts the absorption spectra of all glass samples. The absorption spectrum of the glass sample free from Er^{3+} ions doesn't have any transition band.

The first addition of Er$_2$O$_3$ in bismuth germanium glasses causes a range of Er^{3+} absorption transitions, which translate from the $^4I_{15/2}$ ground state to various excited states due to the f—f transition. The resolved bands in the 400–2000 nm range arise from the $^4I_{15/2}$ ground state to several excited states [7, 14–17] as $^4F_{7/2}$, $^2H_{11/2}$, $^4S_{3/2}$, $^4F_{9/2}$, $^4I_{9/2}$, $^4I_{11/2}$, and $^4I_{13/2}$, with center wavelengths of 486, 522, 542, 650, 796, 980, and 1524 nm, respectively.

Fig. 3 Effect of Er$_2$O$_3$ content on vibration groups resulting from broadband analysis from 850 to 1200 cm^{-1}
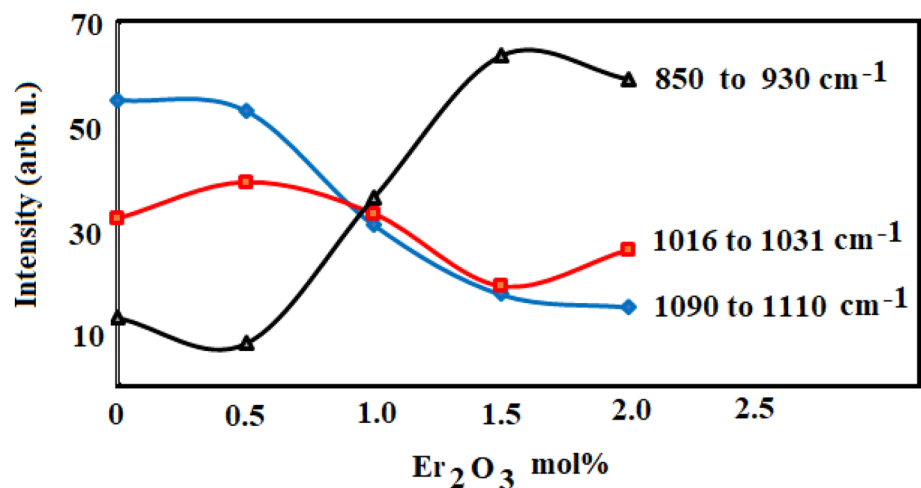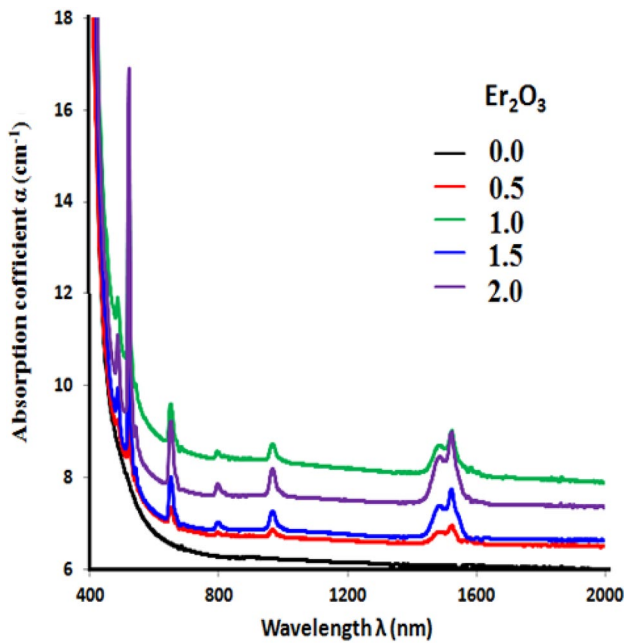
Fig. 4 the optical absorption of glass sampled doped with different concentrations of Er_2O_3

3.4 Judd–Ofelt parameters

The intensity of the optical absorption line of Ln^{3+} ions is used in the modified Judd–Ofelt theory to determine the laser and optical characteristics of ions in crystals and glass [18]. The Judd–Ofelt hypothesis aids in determining the oscillator strength empirically. According to the following relationship [19]:

$$f_{exp} = 4.32 \times 10^{-9} \int \varepsilon(\nu) d\nu \tag{1}$$

$\varepsilon(\nu)$ is the molar absorbance of the peaks at a wave number (cm^{-1}).

The experimental oscillator strength of an electronic transition contains the electric and magnetic dipole strengths.

The magnetic dipole's intensity is determined by the properties of the rare-earth ion, not by the host. Magnetic dipole transitions have a lower probability of occurring than electric dipole transitions. The experimental oscillator line strength determines using [2, 17, 20, 21]:

$$fcal = \frac{8\pi^2 mc(n^2 + 2)^2}{3h\lambda(2J+1)9n} \sum_{(t=2,4,6)} \Omega_t \left(\psi J \left\| U^\lambda \right\| \varphi' J' \right)^2 \tag{2}$$

where λ is the wavelength (nm) of each transition from the ground state (J) to the excited state (J'), **c** is the velocity of light in a vacuum, **m** is an electron's rest mass, Ω_t is the Judd–Ofelt parameters, **n** is the refractive index, **h** is plank's constant, and U^λ is a doubly reduced matrix element.

The fit quality between the experimental and estimated oscillator strengths is determined by the root mean square deviation (δ_{rms}). The following relationship is used to calculate δ_{rms}:

$$\delta_{rms} = \left[\frac{\sum(fexp - fcal)^2}{N-3} \right]^{\frac{1}{2}} \tag{3}$$

The total number of energy levels is **N**. In Table 1, f_{exp}, f_{calc}, and δ_{rms} are calculated and tabulated. The δ_{rms} value indicates the fitting between experimental f_{exp} and calculated f_{calc} strength. Furthermore, using Judd–Ofelt's theory, intensity parameters JO $\Omega\lambda$ (2, 4, and 6) for all samples are calculated and presented in Table 1.

For all glass samples, the values of Judd Ofelt's parameters have a $\Omega_2 > \Omega_6 > \Omega_4$ trend. The higher the value of the Ω_2 intensity parameter, the more asymmetric and covalent the rare-earth ion sites [22]. The value of Ω_λ showed the glass composition containing 1 mol% Er_2O_3 has the largest Ω_2, Ω_4, and Ω_6. The spectroscopy quality factor (χ) is connected to rigidity, laser determination, and amplifier application [16] and is equivalent to the ratio between Ω_4 and Ω_6 [22].

The resulting value was less than 1, indicating a hard glass [7, 23] used in the application of a fiber amplifier with high emission intensity ($^2H_{11/2} \rightarrow {}^4I_{15/2}$) [12, 15, 24] in comparison to the literature [12, 25–28]. The glass composition doped with rare earth causes a wavelength shift, named the nephelauxetic effect. The nephelauxetic effect parameter was determined using the relation [23]:

$$\beta = \nu_c / \nu_a \tag{4}$$

where ν_c is the wave number of the Er^{3+} ion in the host and ν_a is the wave number of the Er^{3+} ion in aqua ions.

The bonding parameter is calculated using the formula $\delta = (1-\beta')/\beta' * 100$ where β' is the average of nephelauxetic. The bonding parameter determines the type of bonding between rare-earth ions and their environment. ν_a, ν_c, β, β', and δ are calculated and tabulated in Table 2.

The band position appears in the same place in Fig. 3, and the negative sign of the value denotes the ionic link between Er_2O_3 ions and the surrounding host.

The value of band gap energy E_{opt} (energy excites the electron from the top of the valance band to the bottom of the conduction band) indicates the bridging and non-bridging oxygen formed in the glass structure.

The optical band gap determines by drawing the relationship between the absorption coefficient and $(\alpha h\nu)^2$ [Tauc plots] with $h\nu$, as shown in Fig. 5. Table 3 summarizes and tabulates the results gathered.

Table 3 shows that the sample without Er has a higher E_{opt} value. The value of E_{opt} decreases with the increase in

Table 1 The Fexp, Fcal, δ, and Judd Ofelt parameter (Ω2, Ω4, Ω6) calculation

Peak position		$0.5\ Er_2O_3$		$1\ Er_2O_3$		$1.5\ Er_2O_3$		$2.0\ Er_2O_3$	
λ (nm)	E (ev)	F_{exp} E-6	F_{calc} E-6	F_{exp} E-6	F_{calc} E-6	F_{exp} E-6	F_{calc} E-6	F_{exp} E-6	F_{calc} E-6
1524	0.81	4.35	3.94	4.46	4.25	4.27	3.91	4.15	3.88
980	1.26	2.51	1.87	3.97	1.99	2.90	1.85	3.30	1.82
796	1.55	0.561	1.44	0.729	1.67	0.596	1.3	0.658	1.4
650	1.90	4.28	3.77	5.98	5.21	3.96	3.5	4.90	4.28
542	2.28	0.373	1.62	0.515	1.69	0.441	1.62	0.448	1.57
522	2.37	14.8	14.5	17.9	17.9	13	12.9	14.6	14.6
486	2.55	1.96	5.48	2.16	6.19	1.73	5.39	1.75	5.54
450	2.75	0.274	1.12	0.203	1.17	0.155	1.12	0.202	1.09
		δ = 2E-6		**δ = 1.8E-6**		**δ = 1.6E-6**		**δ = 1.78E-6**	
		$\mathbf{\Omega_2 = 6.91E\text{-}20}$		$\mathbf{\Omega_2 = 7.73E\text{-}20}$		$\mathbf{\Omega_2 = 6.12E\text{-}20}$		$\mathbf{\Omega_2 = 6.59E\text{-}20}$	
		$\mathbf{\Omega_4 = 0.842E\text{-}20}$		$\mathbf{\Omega_4 = 1.94\ E\text{-}20}$		$\mathbf{\Omega_4 = 0.597E\text{-}20}$		$\mathbf{\Omega_4 = 1.36E\text{-}20}$	
		$\mathbf{\Omega_6 = 2.93E\text{-}20}$		$\mathbf{\Omega_6 = 2.93E\text{-}20}$		$\mathbf{\Omega_6 = 2.89E\text{-}20}$		$\mathbf{\Omega_6 = 2.80E\text{-}20}$	
	$\mathbf{\Omega_4/\Omega_6}$	**0.288**		**0.662**		**0.206**		**0.484**	

Table 2 The values of νa, νc, β, β', and δ bonding

Transition	$\nu_c\ cm^{-1}$	$\nu_a\ cm^{-1}$	$\beta = \nu_c/\nu_a$
$^4F_{7/2}$	2057	2045	1.006
$^2H_{11/2}$	1915	1915	1.0003
$^4S_{3/2}$	1845	1835	1.005
$^4F_{9/2}$	1538	1525	1.008
$^4I_{9/2}$	1256	1240	1.013
$^4I_{11/2}$	1020	1025	0.995
$^4I_{13/2}$	6561	6600	0.994
β' = 1.003347			
δ = − 0.00334			

As shown in Fig. 2, the glass cuts off the UV and a small strip of the visible region, indicating the possibility of using glass samples as a filter [31].

3.5 Density and molar volume

The glass system's density ρ and molar volume V_m are vital in determining a deep sight at any structural alterations in the glass network formation, density, and molar volume are estimated using the relationships [32].
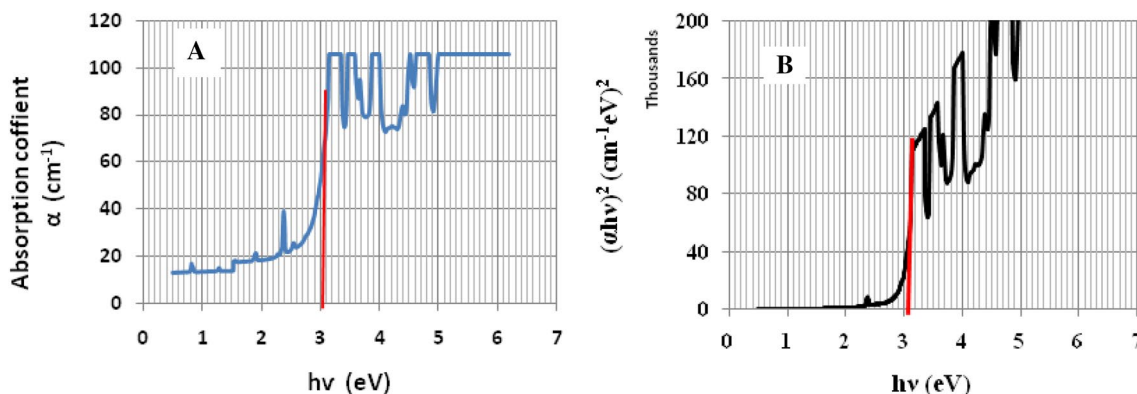
$$\rho = \frac{0.865 Wa}{(Wa - Wb)}\ g\,cm^{-3} \qquad (5)$$

where W_a signifies the sample's weight in the air, W_b denotes the sample's weight in the immersion fluid, and 0.865 is the immersion fluid's density (toluene).

Fig. 5 The transmission of glass composition $40Bi_2O_3$-$60GeO_2$-xEr_2O

Er^{3+}, which indicates an increase in NBOs (non-bridging oxygen) [23, 30].

Table 3 The values of Eopt, Tg, Tx, Tc, Tm, S, HR, n, and Ec of crystallization

Sample	E_{opt}	T_g °C	T_x °C	T_p °C	T_m °C	ΔT °C	HR	n	E_c
0 Er$_2$O$_3$	3.2	480	601.4	640	1009	160	0.43	2.0	109.6
0.5 Er$_2$O$_3$	3.05	490	605	637	1011	147	0.39	2.03	166
1 Er$_2$O$_3$	3.15	495	621.7	664	1009	169	0.48	2.01	133
1.5 Er$_2$O$_3$	3.15	500	643	672	1004	172	0.51	2.01	200.09
2 Er$_2$O$_3$	3.15	497	643	678	999.5	181	0.56	2.01	134.17
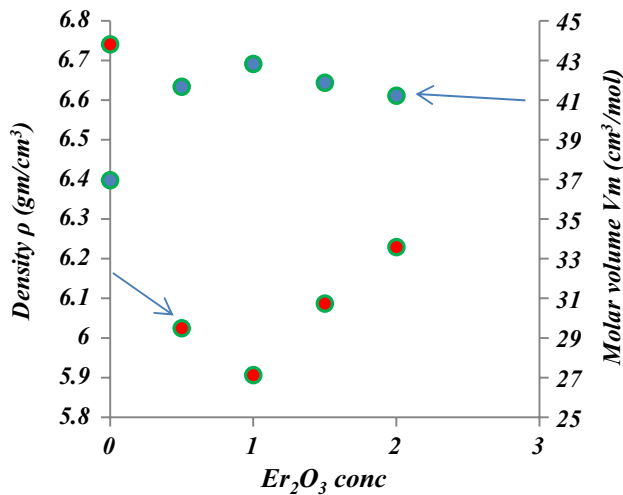
Fig. 6 The density and molar volume calculation of glass samples

Fig. 7 The excitation spectra of Er-doped glass samples at 550nm emission
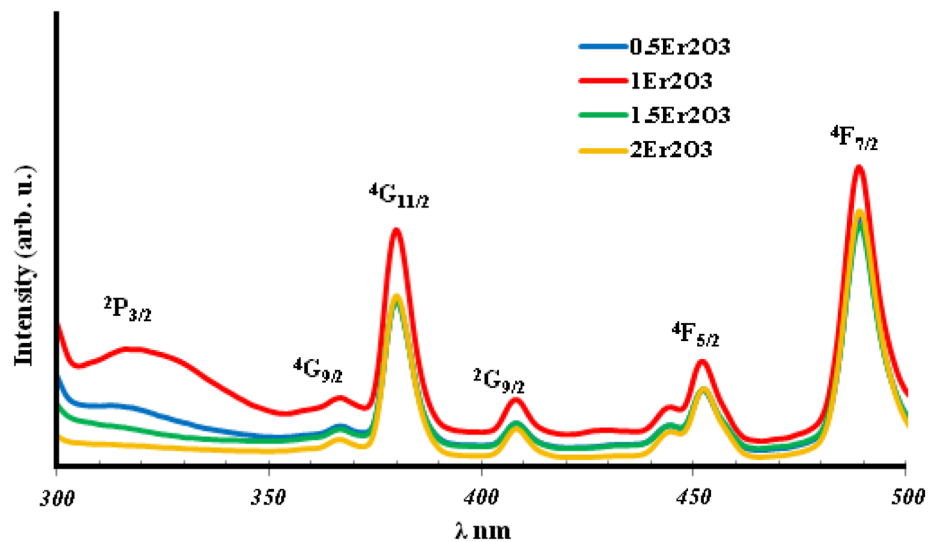
$$V_m = \frac{\sum X_i M_i}{\rho} \, cm^3/mol \qquad (6)$$

where X_i and M_i are the concentration and molecular weight of each oxide.

Figure 6 depicts the connection between density and molar volume as Er concentration rises. It detected a

reversal of the relationship, the density values decreasing up to 1 mol percent Er$_2$O$_3$ and then increasing in the other manner with M_V values. The density changes attributed to the addition of Er^{3+} is due to the breakdown of bonds, and the creation of NBOs, attributed to increased volume as Er ions enter the interstitial site.

Another option is that the RE enters the interstitial site generated by the polymerization of glass [20, 33], which is responsible for the compactness of glass, increasing the molecular weight (MW) of Er$_2$O$_3$.

3.6 Excitation and emission of glass

Figure 7 shows the excitation spectra of Er-doped glass samples at 550 nm emission. Peaks at 317, 368, 381, 410, 453, and 490 nm describe the transition [34, 35] from the ground state $^4I_{15/2}$ to the excited states $^2P_{3/2}$, $^4G_{9/2}$, $^4G_{11/2}$, $^2G_{9/2}$, $^4F_{5/2}$, and $^4F_{7/2}$. The high intensity of two-level transitions at $^4G_{9/2}$ and $^4F_{7/2}$ choose to be the emission energy of the title glass shown in Fig. 8.

It observed the difference in emission energy resulting from different energy peak transitions. The resulting emission spectra showed three peaks at 530, 550,

Fig. 8 The emission spectra of Er-doped glass samples excited at A) 380nm and B) 490nm
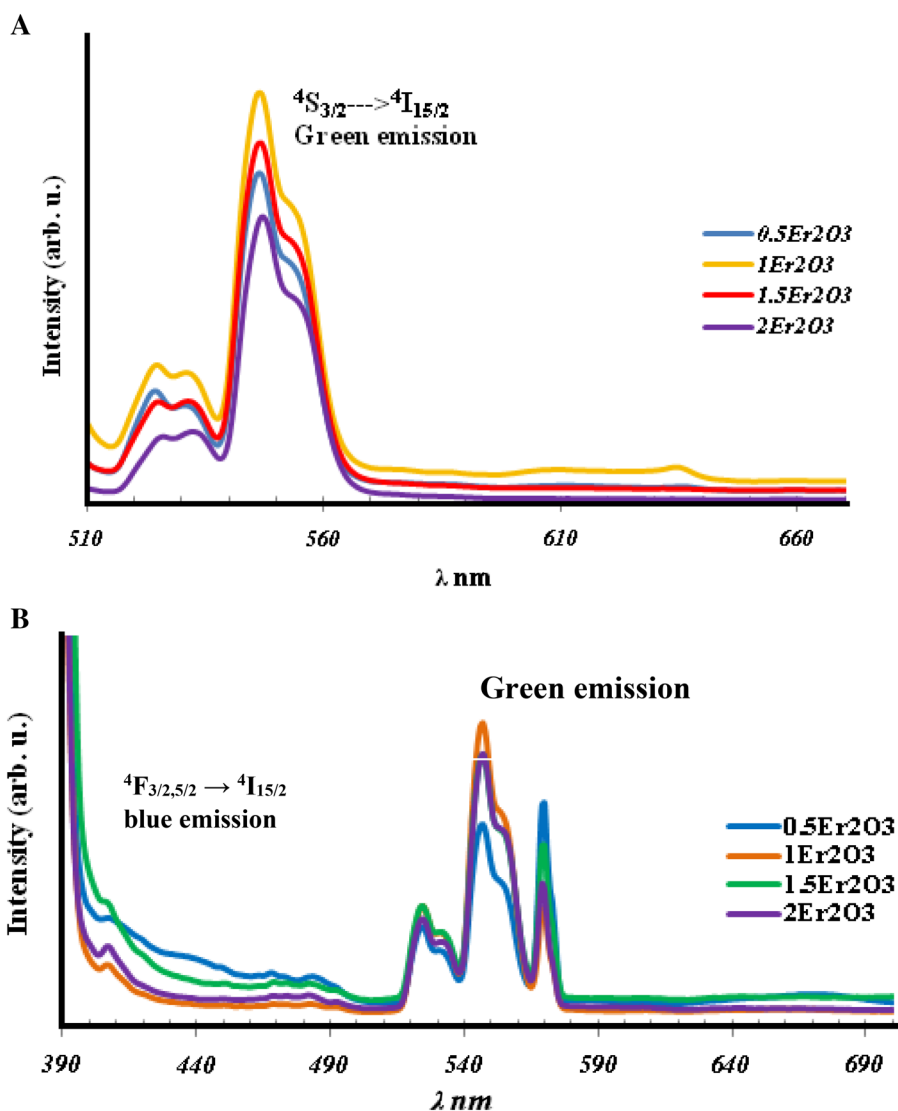
and 639 nm, corresponding to Er^{3+} [12, 23, 25] transitions $^2H_{11/2} \rightarrow {}^4I_{15/2}$ (green emission), $^4S_{3/2} \rightarrow {}^4I_{15/2}$ (green emission), and $^4F_{9/2} \rightarrow {}^4I_{15/2}$ (red emission).

As seen in Fig. 8, emission peaks have two physical qualities. The splitting of the peak results from the stark splitting. The intensity of peak emission increases up to 1 mol% Er_2O_3 and then decreases. This decreases due to the presence of the quenching process caused by non-radiative resonant cross-relaxation at the $^4S_{3/2}$ level [12, 23, 36]. The elimination of red emissions is due to this change [25]. The peak is responsible for the blue emission in the 474–490 region assigned to the $^4F_{3/2,\ 5/2} \rightarrow {}^4I_{15/2}$ transition in another exciting energy at 380 nm [34, 37].

The color coordinates of the CIE chromaticity diagram use to check the variation in light color according to the emission spectra.

As shown in Fig. 9, the CIE chromaticity diagram could be affected in prepared glass mainly by two parameters,

the change of Er concentration and the change of exciting wavelength. The values of chromaticity coordinate listed in Table 4 indicate the samples excited with $\lambda = 489$ nm, used in the emission of green laser [36]. And the emission ranged from white to green light when excited with high energy at 380 nm.

Pandey et al. [37] reported that white light forms from the combination of three colors: blue, green, and red. The sample contains 0.5 mol% close to the expected value of the white light coordinate (0.33, 0.33).

3.7 Thermal properties

DTA curve plays a vital role in the two-point explanation. It explains the glass structure through the T_g value, which is affected by the coordination number, the density of the crosslink, and the bond. strength [11, 38, 39]. On the other hand, it could explain thermal stability. DTA
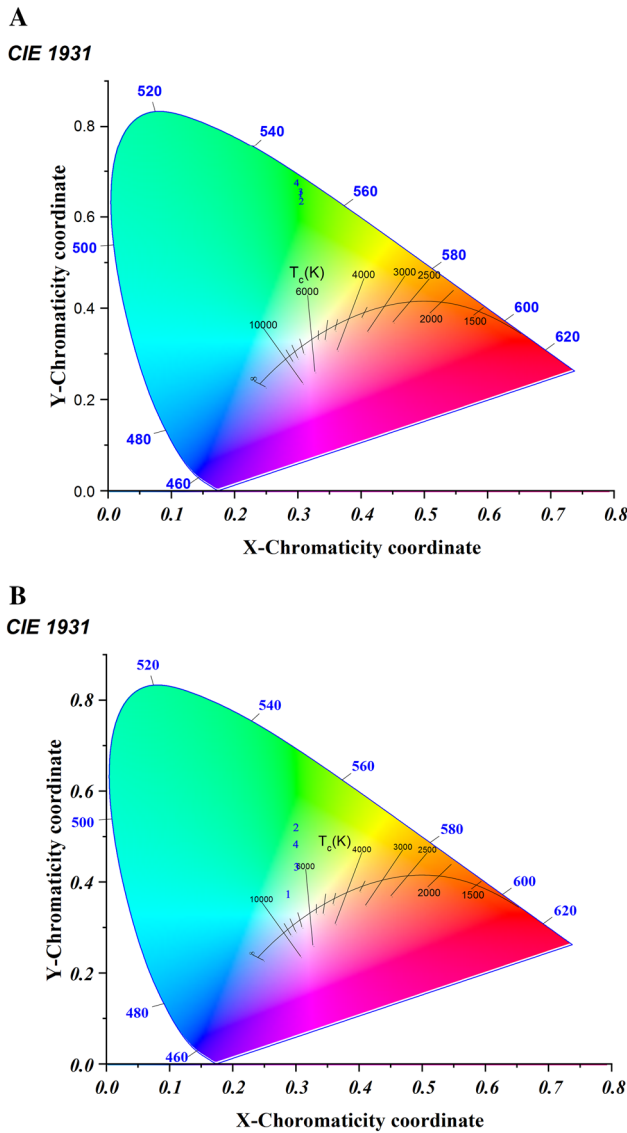
A

B

Fig. 9 The CIE chromaticity coordinates for BiGeEr glasses under excitation wavelength (a) 489 nm and (b) 380 nm

curve characterizes by an endothermic appearance related to annealing, softening, nucleation, and reversible phase transformations determined through T_g and T_m. The exothermic peak represents crystallization and phase change, as defined by the crystallization temperature [40, 41]. The
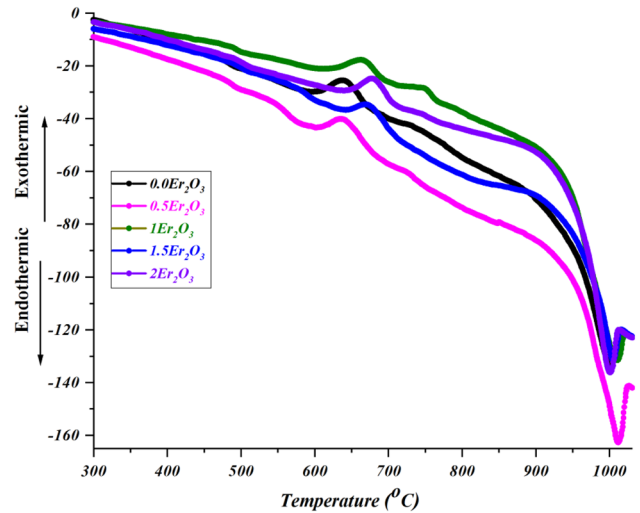

Fig. 10 DTA curves of glass samples.

obtained values tabulated in Table 3 show higher values of T_g compared to glass formed as bismuth boro-tellurite [42], TeO_2-Ga_2O_3-GeO_2 system [43], boron bismuth/fluo-rooxy glass [44], calcium bismuth silicate glass–ceramics [45], Ga-Ge-Sb–Se glass composition [46]. The Tg values increase with the increase of Er concentration as the increase in the compactness of the glass is formed by the presence of Bi in two coordination numbers, BiO_3 and BiO_6 [47], which agrees with the molar volume and FTIR result. Fig. 10 indicates two peaks of different intensities, representing the presence of two crystalline phases, and with the addition of Er_2O_3, the second peak disappears. It interprets as the formation of a single homogenous phase. The thermal stability characterizes by three parameters T_g, the onset of crystallization T_x, and $\Delta T = T_p$-T_g. The higher T_g value could indicate glass has a higher damage threshold due to the transmitted high-power pump, and the higher thermal stability (ΔT is larger than 100 °C) [42, 48] indicate a wide range of working temperatures for the benefit of fiber drawing [49, 50].

Another parameter is the Hrupy parameter $HR = (T_p$-$T_g)/(T_m$-$T_p)$ [38], which comes from a relationship that shows the glass's stability and anti-crystallization ability to form [51, 52].

Relatively such a high value of activation energy for the crystallization, resistance of nucleation and high thermal

Table 4 Chromaticity coordinated of glass, glass ceramic samples and decay lifetime

Sample	$\lambda_{exc} = 489$	$\lambda_{exc} = 380$	Heat treatment		
			$\lambda_{exc} = 380$	$\lambda_{exc} = 522$	τ_{avg} ms
0.5 Er	(0.302, 0.652)	(0.285, 0.377)	(0.233, 0.406)	(0.294, 0.70)	**41.568**
1Er	(0.303,0.636)	(0.298,0.522)	(0.227, 0.392)	(0.293, 0.697)	**7.279**
1.5Er	(0.302,0.657)	(0.299,0.436)	(0.241, 0.442)	(0.295, 0.694)	**7.183**
2Er	(0.296,0.676)	(0.298,0.486)	(0.232, 0.405)	(0.299, 0.690)	**57.052**

Bold average values of decay time τ_{avg}

Fig. 11 Gass samples of different rates ——5, ——10, ——20, and ——30
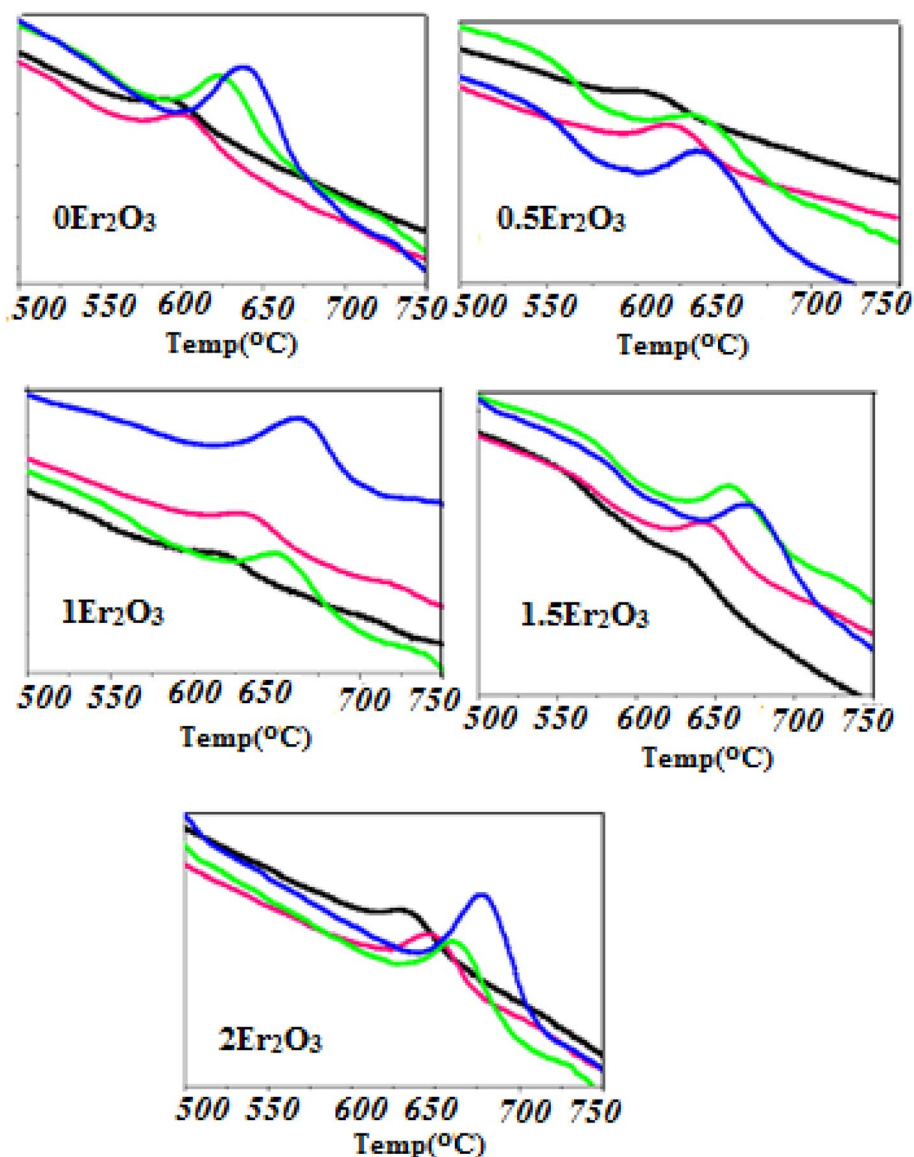
stability for glass samples under study indicates the glass promises for high-powered optoelectronic device applications [53].

The crystallization mechanism of glass is studied using the kinetic parameters obtained from DTA data. Fig. 11 shows the DTA curve for the glass samples at different rates at 5, 10, 20, and 30 °C/min. Fig. 11 shows that the peak of crystallization temperature becomes sharp and shifts to a higher temperature with the increase in the heating rate [54]. Figs. 12, 13.

The activation energy of crystallization can calculate using various approaches [52, 54–56]. The activation energy of crystallization glass samples under investigation is determined using the Augis and Bennett method.

$$Ln\,(\alpha/T_P) \; = \; -\frac{E_C}{RT_p} + Lnk_0 \qquad (7)$$

where α is the heating rate, T**p** is the crystallization temperature, R is the gas constant, and k**o** is a constant.

The relationship between *ln (α /Tp)* and *1000/Tp* (Fig. 12) gives a straight line, and from the slope, the value of the activation energy is determined and tabulated in Table 3.

Ozawa equation used to calculate Avrami coefficient (r) according to [54]:

$$Ln\,[-Ln(1-x)] \; = \; -r\,ln\,\alpha \; + \; const. \qquad (8)$$

X is the crystallization fraction calculated using the equation *X=(A_T /A)*, and *A_T* is the partial area at a given temperature. *A* is the total area of exothermic crystallization [57].

Fig. 12 The relationship between ln (α /Tp) and 1000/Tp
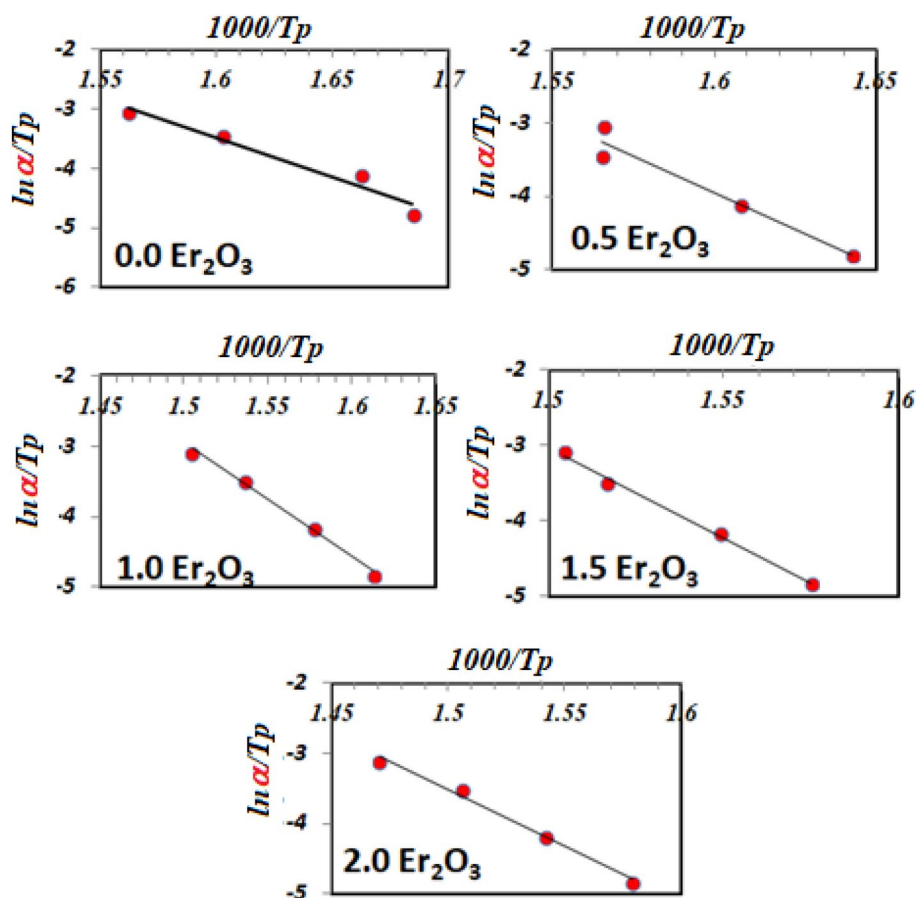
r value determines from the slope of the straight line of the relation between *ln[-ln(1-x)]* and *lnα* (Fig.13). The *r* values of the prepared glass samples are 1.9, 1.56, 1.56, 1.89, and 1.54. This value indicates that surface crystallization occurred during one-dimensional growth [54, 58].

3.8 XRD of heat-treated samples

Young [59] investigated the heat-treated glass sample (40Bi_2O_3-60GeO_2 mol %) at 521 and 584 °C. The formation of two phases, Bi_2GeO_5 and $Bi_4Ge_3O_{12}$, can be observed. They also formed glass samples with different concentrations of Bi_2O_3 and GeO_2 containing B_2O_3 or Sm_2O_3 mol %, and by thermally treating them at 630 °C, the crystalline phase of the $Bi_4Ge_3O_{12}$ cube formed.

The current study comprises adding different amounts of Er_2O_3 mol % to a 40 Bi_2O_3-60 GeO_2 mol % glass sample manufactured and heat-treated at 650 °C. The development of crystals causes bulk samples to become opaque. According to the XRD study, the only $Bi_4Ge_3O_{12}$ phase developed is isolated tetrahedral GeO_4, and distorted BiO_6 units make up the BGO crystal structure [59, 60]. Fig. 14 shows the

XRD patterns at room temperature for materials generated by heat treatments at 650 °C for 5 h. The $Bi_4Ge_3O_{12}$ crystalline phase (ICDD: 01–074-6243) ascribed to the XRD peaks seen in samples free of Er^{3+} ions and containing Er_2O_3.

The size of particles computed using the Scherrer equation [9] was between 55 and 73 nm. Another approach considers all diffraction peaks, although the findings are relatively similar.

3.9 FTIR of heat-treated samples

FTIR measurements demonstrate any structural changes when the glass samples are converted to glass–ceramic using heat treatment (Fig. 15). As well as compare the results of heat treatment on the glass structure.

The range of 490–540 cm^{-1} indicates a significant quantity of crystallization ($Bi_4Ge_3O_{12}$ phase). [60], which is consistent with the XRD results.

The band at 540 to 830 cm^{-1} becomes wide and more intense than observed in the glass samples, representing the overlapping structure of the BiO_6 and GeO_4 compositions.

Fig. 13 The relation between $\ln[-\ln(1-x)]$ and $\ln\alpha$
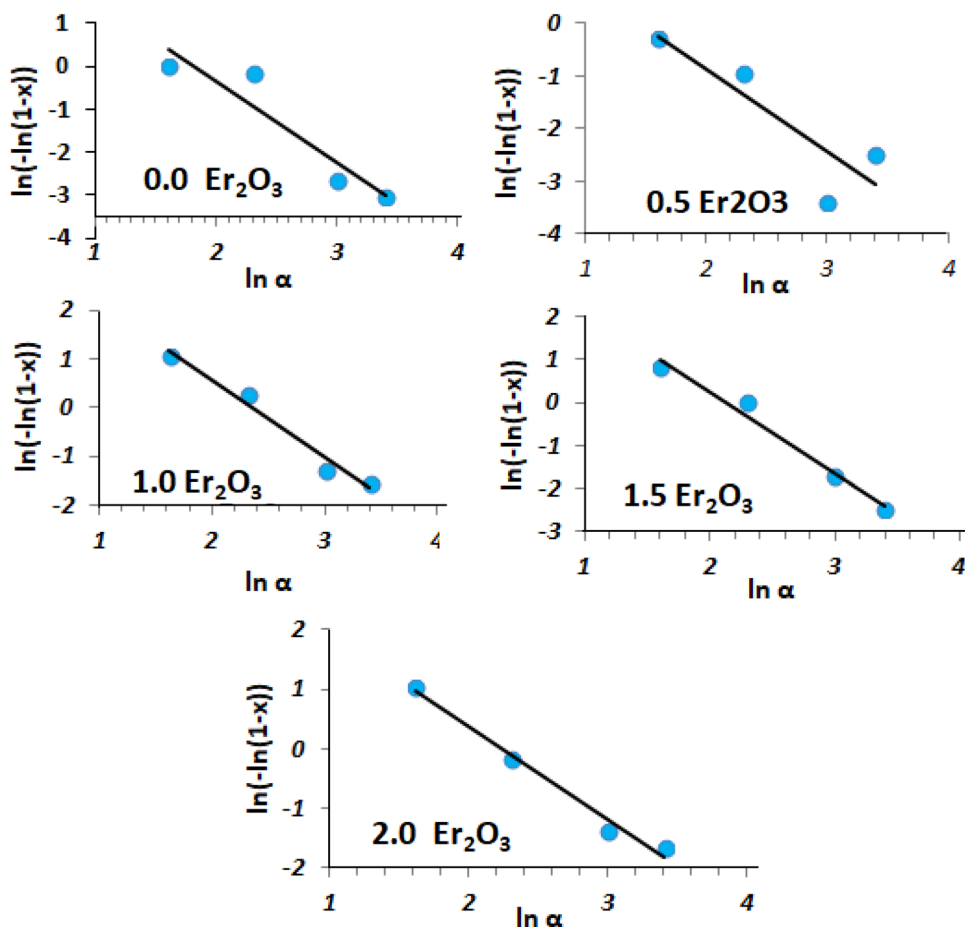
Heat treatment separates the band created in glass samples ranging from 830 to 1100 cm^{-1} into two bands, broadening and intensifying it. An increase in BiO$_6$ groups causes a sharp band at 870 cm^{-1}. Bi-O-Bi bonds or the interaction between Bi-O-Ge [1] cause the band at 1110 cm^{-1}.

The formation of symmetric vibrations of hydrogen bond (OH) groups is due to the addition of a modifier or change of the bismuth from the former to the modifier in the glass network, which breaks the bridging oxygen and leads to the formation of NBO atoms. The formation of NBO leads to give vacant oxygen atoms and these oxygen atoms will take part in the formation of OH groups. And the high concentration of OH groups in glass can increase the crack growth, impurities and trapping and leads to a decrease in the overall strength and luminous intensity of the glass. The OH content present in a glass can be evaluated using the following formula [61, 62]:

$$\alpha_{OH} = \frac{\ln\left(\frac{\tau_o}{\tau_D}\right)}{L} \tag{9}$$

Here, τ_o is the maximum transmission, τ_D is the transmission at 3000 cm^{-1} and L is the thickness of the glass sample.

The OH content can be calculated according to the following equation:

$$\text{OH content (ppm)} = 30 \text{ x } \alpha_{OH} \tag{10}$$

The estimated OH content for the glass samples under study is found between 94 to 102 ppm, which is relatively low when compared with the other glasses such as LBTAF (120 ppm), LHG-8 (773 ppm), GeS2 (175.5 ppm) and KBS (133 ppm) [63–66].

Hence present systems of glasses are quite suitable for visible photonic applications.

3.10 Excitation and emission of heat-treated sample

Due to the importance of Bi$_4$Ge$_3$O$_{12}$ phase formation in glass ceramics, it uses in laser host crystal and scintillation detector applications [67, 68].

This phase could exhibit green emission [69]. Fig. 16 displays the excitation curve for the glass–ceramic sample doped with 2 mol % Er.
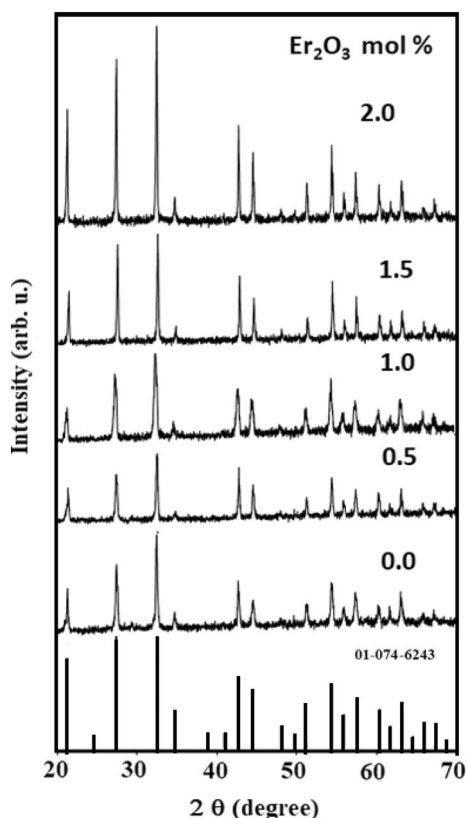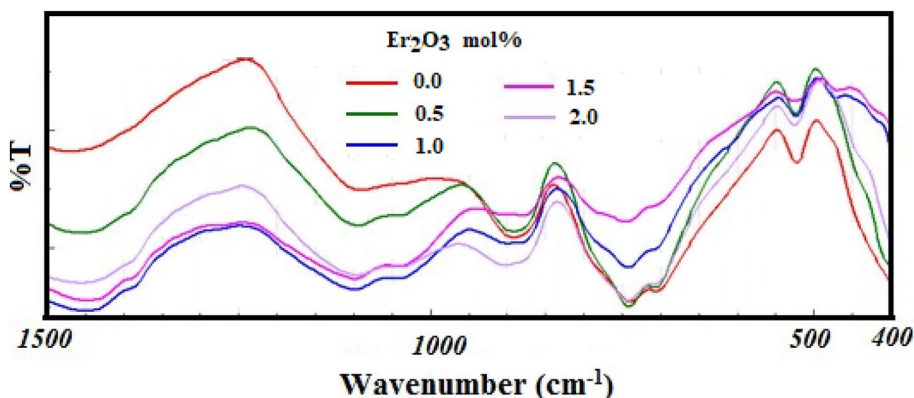
Fig. 14 XRD of heat-treated glass samples at 650 °C

Figure 16 shows the same exciting peaks in the glass sample curve (Fig. 7) in addition to the band at 522 nm. The intense emission obtains by exciting the sample with the energy corresponding to the prominent excitation band. Furthermore, glass–ceramic excited at 380 nm and 522 nm emit green light, whereas glass–ceramic excited at 380 nm emit blue light as shown in Fig. 17A and 17B.

The CIE chromaticity program shows the emission color. The x–y color parameters calculate and included in Table 4. From Table 4, the emission difference is due to the difference in the emitted wavelengths. Excitation at 522 nm coordinates the green emission chromaticity. The apparent

excitation at 380 nm coordinates the blue-green emission chromaticity. Figs. 18A and18B.

3.11 lifetime decay

The lifetime is an important factor for potential laser materials. The fluorescence decay curve of Er^{3+} ion excited at 380 nm and monitored at 522 nm at room temperature of the present samples was measured and is shown in Fig. 19. The decay curves have deviated from single exponential, the decay profile is found to be biexponential for all samples except the sample containing 1.5 mol% Er_2O_3 follow single exponential decay. The bi-exponential nature may be because of the reason that the energy transfer from excited donor ion to unexcited acceptor ion transpires. The intensity of luminescence can be articulated as follows [66]:

$$I = I_o + A_1 \exp\left(-\frac{t}{\tau_1}\right) + A_2 \exp\left(-\frac{t}{\tau_2}\right) \tag{11}$$

where, I_0 is the intensity at t = 0, and I is intensity at time t, A_1 and A_2. are the amplitudes of decay constants and τ_1 and τ_2 are the luminescence lifetimes for fast and slow channels of decay, respectively. The average values of decay time are calculated by using the formula given as [66]:

$$\tau_{avg} = \frac{\left(A_1\tau_1^2 + A_2\tau_2^2\right)}{\left(A_1\tau_1 + A_2\tau_2\right)} \tag{12}$$

The average lifetime values for Er^{3+} ion-doped glasses are inset in Table 4 and are shown in Fig. 18. It can be seen the average lifetime decreases with an increase in **Er^{3+}** ion concentration signifying the energy transfer between **Er^{3+}**— **Er^{3+}** ions [71–73].

4 Conclusion

Bismuth germanium glass systems doped with **Er^{3+}** ions were studied using different techniques and concluded that:

Fig. 15 FTIR of heat-treated glass samples at 650 °C

Fig. 16 The Excitation spectra of glass–ceramic doped with 2 mol% Er measured at an emission wavelength of 550 nm
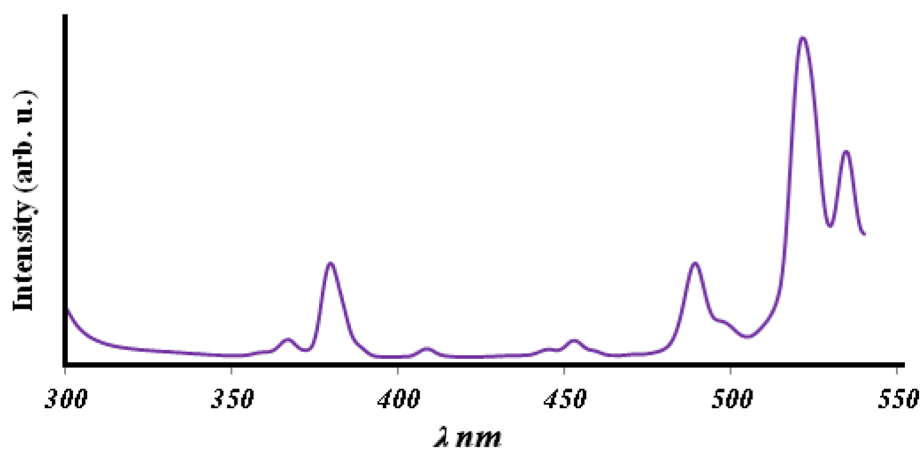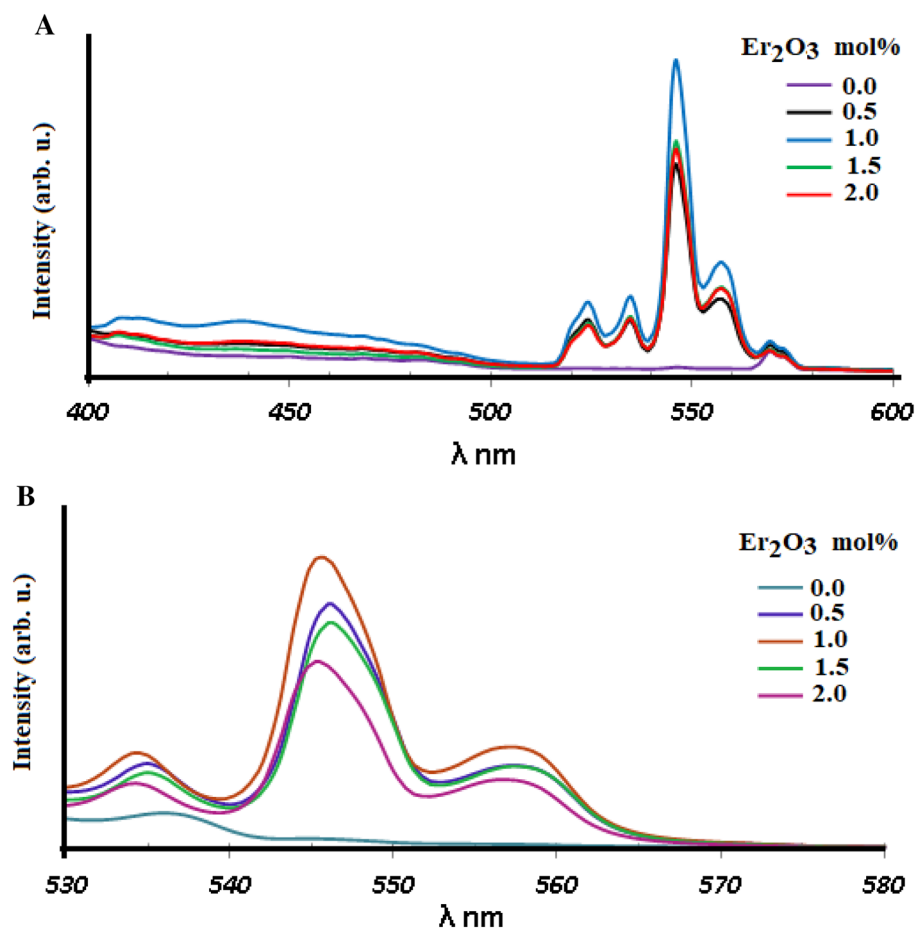

Fig. 17 The emission spectra of glass–ceramic samples at two excitation wavelengths λ_{exc} at **A** = 380 nm and **B** = 522 nm

1. The pyramidal [BiO_3] octahedral [BiO_6] units and GeO_4 tetrahedral units are the glass network of samples under study.

2. The Ω_2 and Ω_4/Ω_6 values were higher for the sample containing one mol% Er^{3+}, which was attributed to the covalent nature and suggested it as a better glass for laser material applications.

3. The XRD spectra show the $Bi_4Ge_3O_{12}$ crystalline phase (50–73 nm size nano-crystals) participating in the glass samples.
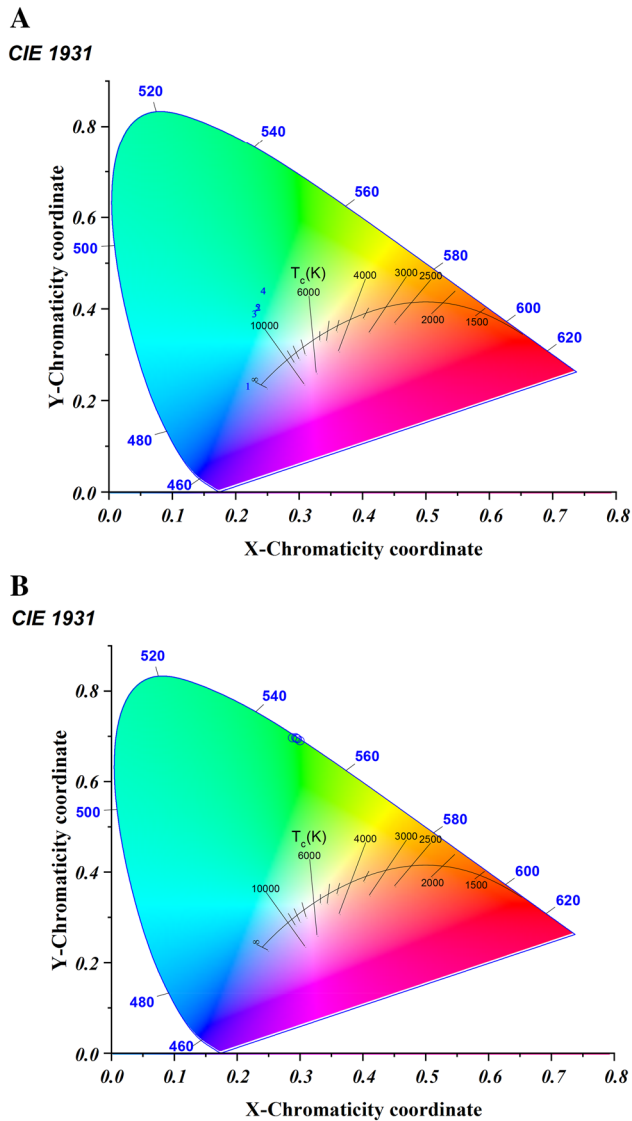
A

CIE 1931

B

CIE 1931

Fig. 18 The CIE chromaticity coordinates for glass–ceramic samples under excitation wavelength (**A**) 380 nm and (**B**) 522 nm

4. The values of the chromaticity coordinates refer to the samples excited at 489 nm used for green laser emission, while excited at 380 nm used for emission ranging from white light to green emission.
5. The luminescence quenching of > 1 mol of Er^{3+} ion concentration occurs under both excitation in the prepared glass–ceramic samples due to the formation of a non-radiative cross-relaxation.
6. Based on the structure study, OH content, thermal analysis, emission lifetime and CIE coordinates, it is concluded that the Er3 + ions doped Bismuth germanium glasses are suitable for green and blue optoelectronics device applications.
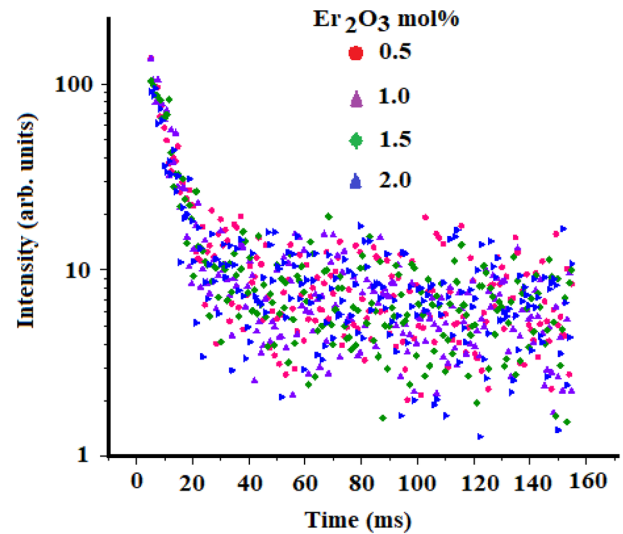

Fig. 19 The decay curve of Er^{3+} doped bismuth germinate glass–ceramics at room temperature

Data availability The data that support the findings of this study are available from the corresponding author upon reasonable request.

Declarations

Conflict of interest No conflict of interest.

Ethical approval This paper meets the ethical standards of this journal.

Consent to participate All authors agree with the review of this paper in this journal.

References

1. P. Pascuta et al., The local structure of bismuth germanate glasses and glass ceramics doped with europium ions evidenced by FT-IR spectroscopy Vib. Spectrosc. **48**, 281–284 (2008)

2. Q. Nie et al., Upconversion luminescence of Er3+/Yb3+-codoped natrium–germanium–bismuth glasses. J. Phys. Chem. Solids **67**, 2345–2350 (2006)

3. S. Arunkumar, K. Marimuthu, Spectroscopic properties of Er3+ doped bismuth leadtelluroborate glasses for 1.53 μm optical amplifiers. J. Alloys Compd. **627**, 54–68 (2015)

4. S. Polosan, Crystallisation of bismuth germanate glasses below their glass transition temperature. J. Non. Cryst. Solids **472**, 55–60 (2017)

5. P. Beneventi et al., (1995) A Raman study of $Bi_4(Ge_xSi_{1-x})_3 O_{12}$ crystals Solid State Commun, **93**, 143–146

6. Y. Chen et al., Spectroscopic properties of Er^{3+} ions in bismuth borate glasses Opt. Mater. (Amst) **25**, 271–278 (2004)

7. S. Sanghi et al., Effect of Bi_2O_3 on spectroscopic and structural properties of Er^{3+} doped cadmium bismuth borate glasses spectrochim. Acta Part A Mol. Biomol. Spectrosc. **83**, 94–99 (2011)

8. S. Polosan, F. Nastase, M. Secu, Structural changes during the crystallization of the $Bi_4Ge_3O_{12}$ glasses. J. Non. Cryst. Solids **357**, 1110–1113 (2011)

9. S. Polosan, A. Galca, M. Secu, Band-gap correlations in $Bi_4Ge_3O_{12}$ amorphous and glass-ceramic materials. Solid State Sci. **13**, 49–53 (2011)

10. X. He et al., Abnormal near-infrared luminescence property of bismuth doped calcium germanate glasses. J. Non. Cryst. Solids **402**, 166–171 (2014)

11. M. Farouk et al., Optical absorption and structural studies of bismuth borate glasses containing Er^{3+} ions. J. Non. Cryst. Solids **371–372**, 14–21 (2013)

12. J. Bhemarajam et al., Spectroscopic and optical investigations on Er^{3+}/Yb^{3+}co-doped bismuth–boroleadlithium glasses for solid state laser applications. Opt. Mater. **122**, 111657 (2021)

13. R. Wang et al., Structure and luminescent property of Er^{3+}- doped germanate glasses. J. Non. Cryst. Solids **383**, 200–204 (2014)

14. M. Kumar et al., Luminescence and gain characteristics of 1.53 μm broadband of Er^{3+} in lead telluroborate glasses. J. Lumin. **142**, 128–134 (2013)

15. A. Madhu et al., Er^{3+}-ions doped lithium-bismuth-boro-phosphate glass for 1532 nm emission and efficient red emission up conversion for telecommunication and lasing applications. J. Non. Cryst. Solids **495**, 35–46 (2018)

16. S. Nian et al., Optical properties of Er^{3+}/Yb^{3+} co-doped bismuth calcium borate glass system for NIR lasers and fiber amplifiers. J. Lumin. **194**, 440–445 (2018)

17. T. Wei et al., Structure and spectroscopic properties of Er^{3+} doped germanate glass for mid-infrared application. Solid state sci. **31**, 54–61 (2014)

18. A. Ghosh, R. Debnath, Judd-Ofelt analysis of Er+3 activated lead free fluoro–tellurite glass Opt. Mater. (Amst) **31**, 604–608 (2009)

19. E. Mohamed et al., Crystallization kinetics and optical properties of titanium–lithium tetraborate glass containing europium oxide. Appl. Phys. A Mater. Sci. Process. **123**, 479 (2017)

20. D. Ramteke, R. Kroon, H. Swart, Infrared emission spectroscopy and upconversion of $ZnO-Li_2O-Na_2O-P_2O_5$ glasses doped with Nd3 + ions. J. Non. Cryst. Solids **457**, 157–163 (2017)

21. I. Khan et al., Photoluminescence and white light generation of Dy_2O_3 doped $Li_2O-BaO-Gd_2O_3-SiO_2$ for white light LED. J. Alloys Compd. **774**, 244–254 (2019)

22. Sk. Mahamuda et al., Spectroscopic properties and luminescence behavior of Nd^{3+} doped zinc alumino bismuth borate glasses. J. Phys. Chem. Solids **74**, 1308 (2013)

23. J. Bhemarajam et al., Spectroscopic studies on Er^{3+} ions incorporated bismuth borolead lithium glasses for solid state lasers and fiber amplifiers Opt. Mater. (Amst) **113**, 110818 (2021)

24. N. Vijaya et al., Optical characterization of Er^{3+}-doped zinc fluorophosphate glasses for optical temperature sensors. Sensors Actuators B Chem. **186**, 156–164 (2013)

25. K. Annapoorani et al., Influence of Er^{3+} ion concentration on spectroscopic properties and luminescence behavior in Er^{3+} doped Strontium telluroborate glasses. J. Lumin. **171**, 19–26 (2016)

26. P. Babu et al., Optical spectroscopy, 1.5 μm emission, and upconversion properties of Er^{3+}-doped metaphosphate laser glasses. J. Optical Society of America B **24**, 2218–2228 (2007)

27. S. Saleem et al., Erbium-doped fluoroborate glasses for near infrared broadband amplifiers *Int*. J. Appl. Glas. Sci. **2**, 215–221 (2011)

28. B. Jamalaiah et al., Visible and near infrared luminescence properties of Er^{3+}-doped LBTAF glasses for optical amplifiers. Opt. Mater. (Amst) **34**, 861–867 (2012)

29. M. Mariyappan et al., Effect Bi_2O_3 on the physical, structural and radiation shielding properties of Er^{3+} ions doped bismuth sodiumfluoroborate glasses. J. Non. Cryst. Solids **499**, 75–85 (2018)

30. I. Kashif, A. Ratep, Effect of copper oxide on structure and physical properties of lithium lead borate glasses Appl. Phys. A **120**, 1427–1434 (2015)

31. I. Kashif, A. Ratep, Effect of copper addition on BO_4, H_2O groups and optical properties of lithium lead borate glass. Opt. Quantum Electron. **49**, 231 (2017)

32. I. Kashif, A. Ratep, Red and green emission from chromium metal or oxide on co-doped lithium tetraborate glass. Opt. Quantum Electron. **48**, 516 (2016)

33. D. Ramteke, R. Gedam, H. Swart, Physical and optical properties of lithium borosilicate glasses doped with Dy^{3+} ions Phys. B Condens. Matter **535**, 194–197 (2017)

34. G. Chandrashekaraiah et al., Correlation between non-linear optical parameter and structure of $Li_2B_4O_7$ glasses doped with Er^{3+} ions. J. Non. Cryst. Solids **531**, 119843 (2020)

35. L. Mukhopadhyay et al., 980 nm excited $Er^{3+}/Yb^{3+}/Li^+/Ba^{2+}$: $NaZnPO_4$ upconverting phosphors in optical thermometry. J. Lumin. **187**, 368–377 (2017)

36. C. Kesavulu et al., Influence of Er^{3+} ion concentration on optical and photoluminescence properties of Er^{3+}-doped gadolinium-calcium silica borate glasses. J. Alloys Compd. **683**, 590–598 (2016)

37. A. Pandey et al., Enhanced upconversion and temperature sensing study of Er3+–Yb3+ codoped tungsten-tellurite glass. Sensors Actuators B Chem. **202**, 1305–1312 (2014)

38. I. Kashif, A. Ratep, S. El-Mahy, Structural and optical properties of lithium tetraborate glasses containing chromium and neodymium oxide Mater. Res. Bull. **89**, 273–279 (2017)

39. A. Fayad et al., Influence of CuO on crystallization and electrical properties of B_2O_3-Bi_2O_3-GeO_2-CaF_2 glass system for thermoelectronic applications. J. Non. Cryst. Solids **544**, 120185 (2020)

40. S. Abdel-Hameed, Y. Hamdy, H. Sadek, Characterization and Luminescence Properties of Mn-Doped Zinc Borosilicate Glasses and Glass-Ceramics Silicon. 11, 1185-1192 (2019)

41. X. Song et al., Broadband ~1.8 μm emission characteristics of Tm3+-doped bismuth germanate glass based on Ga2O3 modification. J. Non. Cryst. Solids **557**, 120575 (2021)

42. N. Elkhoshkhany et al., Optical properties and crystallization of bismuth boro-tellurite glasses. J. Non. Cryst. Solids **476**, 15–24 (2017)

43. A. Marczewska, M. Środa, Spectroscopic and thermal study of a new glass from TeO_2–Ga_2O_3–GeO_2 system. J. Mol. Struct. **1164**, 100–108 (2018)

44. S. Li et al., Study on preparation and properties of boron bismuth/fluorooxy glass and glass-ceramics. J. Non. Cryst. Solids **561**, 120749 (2021)

45. R. Guntu et al., Structure, and opto-dielectric investigations of Cu^{2+}-doped calcium bismuth silicate glass ceramics. Opt. Mater. (Amst) **113**, 110876 (2021)

46. E. Karaksina et al., Effect of Ge-rich Ga-Ge-Sb-Se glass composition on the optical and thermal properties Opt. Mater. (Amst) **104**, 109943 (2020)

47. S. Abdel-Hameed, A. Fathi, M. Eltohamy, Structure, optical and electrical behaviour of x(2Bi2O3.MnO). (10–x)B2O3 glasses. J. Non. Cryst. Solids **510**, 71–80 (2019)

48. M. Peng et al., Bismuth-doped zinc aluminosilicate glasses and glass-ceramics with ultra-broadband infrared luminescence. Opt. Mater. (Amst) **29**, 556–561 (2007)

49. H. Sun et al., Effect of chloride ions' introduction on structural, thermal stability, and spectroscopic properties in $Yb^{3+}Er^{3+}$-codoped germanate-bismuth-lead glasses. J. Opt. Soc. Am. B **22**, 2601 (2005)

50. G. Zhao et al., Broadband near-IR emission and temperature dependence in Er/Tm co-doped Bi_2O_3-SiO_2-Ga_2O_3 glasses. Phys. B Condens. Matter **407**, 4622–4626 (2012)

51. M. Mhareb et al., Effect of Dy_2O_3 impurities on the physical, optical and thermoluminescence properties of lithium borate glass. J. Lumin. **177**, 366–372 (2016)

52. M. Abdel-Rahim et al., Kinetic study of non-isothermal crystallization of BixSe100- x chalcogenide glasses. Phys. B Condens. Matter **403**, 2956–2962 (2008)

53. A.S. Ravia, Rao, Effective sensitization of Eu3+ visible red emission by Sm3+ in thermally stable potassium zinc alumino borosilicate glasses for photonic device applications. J. Lumin. **244**, 118689 (2022)

54. S. Panyata et al., Non-isothermal crystallization kinetics of bismuth germanate glass-ceramics Ceram. Int. **43**, S407–S411 (2017)

55. K. Matusita, T. Komatsu, R. Yokota, Kinetics of non-isothermal crystallization process and activation energy for crystal growth in amorphous materials. J. Mater. Sci. **19**, 291–296 (1984)

56. J. Augis, J. Bennett, Calculation of the Avrami parameters for heterogeneous solid state reactions using a modification of the Kissinger method. J. Therm. Anal. **13**, 283–292 (1978)

57. I. Kashif, A. Soliman, A. Sanad, Effect of grain size on the crystallization kinetics of copper vanadate glasses Physics and Chemistry of Glasses. **39**, 195-199 (1998)

58. N. Afify et al., Kinetics study of non-isothermal crystallization in Se0.7-Ge0.2 Sb0.1 chalcogenide glass. J. Non. Cryst. Solids **128**, 269–278 (1991)

59. C. Yang et al., Nano-crystallization and highly oriented crystal line patterning of Sm3+-doped Bi_2GeO_5 and $Bi_4Ge_3O_{12}$ in bismuth germanate-based glasses. J. Non. Cryst. Solids **459**, 116–122 (2017)

60. S. Rojas et al., Influence of ceria addition on thermal properties and local structure of bismuth germanate glasses. J. Non. Cryst. Solids **356**, 2942–2946 (2010)

61. J. Zhang et al., 2.8 µm emission and OH quenching analysis in Ho3+ doped fuorotellurite-germanate glasses sensitized byYb3+ and Er3+. Sci. Rep. **7**, 16794 (2017)

62. X. Fan et al., Spectroscopic properties of 2.7µm emission in Er3+ doped telluride glasses and fibers. J. Alloys Compd. **615**, 475–481 (2014)

63. T. Suhasini et al., An investigation on visible fluorescence characteristics of Ho3+ activated LBTAF glasses. Phys. B **407**, 523–527 (2012)

64. T. Som, B. Karmakar, Nephelauxetic effect of low phonon antimony oxide glass in absorption and photoluminescence of rare-earth ions, Spectrochim. Acta - Part A Mol. Biomol. Spectrosc. **79**, 1766–1782 (2011)

65. B.B. Kale et al., Removal of OH impurities from GeS2 by reactive atmosphere and its glass preparation. Mater. Chem. Phys. **78**, 330–336 (2003). https://doi.org/10.1016/S0254-0584(01)00551-X

66. P.R. Rani et al., Structural, absorption and photoluminescence studies of Sm3+ ions doped barium lead alumino fluoro borate glasses for optoelectronic device applications. Mat. Res. Bull. **110**, 159–168 (2019)

67. S. Kaczmarek et al., Temperature dependence of Bi4Ge3O12 photoluminescence spectra mater. Sci. Pol. **32**, 7–11 (2014)

68. L. Dimesso et al., The crystallization behaviour of bismuth germanate glasses. J. Mater. Sci. **26**, 4215–4219 (1991)

69. F. Rooemond et al., Crystals under laser excitation : excited state. J. Lumin. **33**, 455–486 (1985)

70. S. Kaur et al., Spectroscopic studies of Dy3+ doped borate glasses for cool white light generation. Mat. Res. Bull. **104**, 77–82 (2019)

Publisher's Note Springer Nature remains neutral with regard to jurisdictional claims in published maps and institutional affiliations.